2013-05

Generalized orthogonal wavelet phase reconstuction

Axtell, Travis W.; Cristi, Roberto

Optical Society of America

T.W. Axtell, R. Cristi, "Generalized orthogonal wavelet phase reconstruction," Journal of Optical Society of America, A, v.30, no.5, (May 2013), pp. 859-870.
http://hdl.handle.net/10945/56646

Generalized orthogonal wavelet phase reconstruction

Travis W. Axtell* and Roberto Cristi

Department of Electrical and Computer Engineering, Naval Postgraduate School, Spanagel Hall, Room 437, 833 Dyer Road, Monterey, California 93943-5216, USA
**Corresponding author: twaxtell@nps.edu*

Received October 19, 2012; revised March 13, 2013; accepted March 13, 2013;
posted March 14, 2013 (Doc. ID 178355); published April 12, 2013

Phase reconstruction is used for feedback control in adaptive optics systems. To achieve performance metrics for high actuator density or with limited processing capabilities on spacecraft, a wavelet signal processing technique is advantageous. Previous derivations of this technique have been limited to the Haar wavelet. This paper derives the relationship and algorithms to reconstruct phase with $O(n)$ computational complexity for wavelets with the orthogonal property. This has additional benefits for performance with noise in the measurements. We also provide details on how to handle the boundary condition for telescope apertures.

OCIS codes: (010.1080) Active or adaptive optics; (100.0100) Image processing; (010.7350) Wave-front sensing; (100.7410) Wavelets.
http://dx.doi.org/10.1364/JOSAA.30.000859

1. INTRODUCTION

Closed-loop adaptive optics (AO) systems require an estimate of the wavefront phase to command the 2D controllable deformable mirror actuators [1,2]. Most implemented systems reconstruct the phase at discrete locations called phase points. To simplify system calculations, oftentimes these phase points are registered to actuator locations, then the necessary phase correction is determined for the control law without interpolation.

The AO community has developed several algorithms for wavefront phase reconstruction. Ideally the approaches would

1. Be computationally efficient for a large number of data points,
2. Be robust to measurement noise, and
3. Result in perfect reconstruction of the wavefront using noise-free wavefront sensor data.

The first property is essential for future telescopes that increase the number of actuators or sensor measurements seeking diffraction-limited performance. The second property depends on the mathematical operations performed by the algorithm and, in general, depends on the statistics of the measurements, including correlations. The final property was discussed previously by Southwell [3] and Poyneer *et al.* [4], and the difficulty arises from the pupil geometry interaction with the algorithm.

The original wavefront reconstruction techniques used matrix-vector multiplication [3,5–7] with computational complexity of $O(n^2)$ or higher. Later, the Fourier transform technique was proposed by Freischlad [8], with further refinement by Poyneer *et al.* [4], and has $O(n \log_2 n)$ complexity, limited by the speed of the implementation of the fast Fourier transform for the change of basis. In essence, their treatment of the wavefront sensor measurements as a filtering operation is similar to the concept of this paper, except that their filtering operations occur on the global data set and solve the entire phase surface at once. During the same time period as Poyneer *et al.* [4], Gilles *et al.* [9] produced a multigrid preconditioned conjugate-gradient method with the same computational complexity.

The first $O(n)$ work in accurate wavefront reconstruction was performed by MacMartin, where he developed a multiresolution hierarchic reconstructor [10]. His work downsampled by a factor of 4 or more, and results show that the larger downsampling factor decreases the relative performance and increases the noise multiplier. Our work in this paper uses a downsampling factor of 2, which gives improved performance of the second property.

Additional $O(n)$ work followed, such as that from Gilles [11]. This work was a direct application of a multigrid solver of a minimum-variance reconstructor based on a sparse approximation of the wavefront inverse covariance matrix. Vogel also improved sparse matrix methods [12] and a multigrid least-squares algorithm [13]. Another minimum-variance solver that followed is the fractal iterative method [14,15], which performs a change of basis (using a fractal preconditioner). Minimum-variance reconstruction is an excellent choice, as it is optimal in the sense of maximizing the Strehl ratio [16].

In the last few years, several new wavefront reconstruction algorithms have been proposed. Rosensteiner has produced the cumulative reconstructor, which is a direct integration reconstructor [17]. More recently, de Visser has shown the SABRE algorithm using B-spline basis functions [18].

Wavelets were first applied to wavefront reconstruction by Dowla [19]. This original work did not fully exploit the features of the discrete wavelet transform (DWT) and was an approximation. Hampton and co-workers developed an algorithm that used the complete DWT and were able to perform reconstruction using the Haar wavelet [20,21]. This paper extends on their work to allow for the use of wavelets with the orthogonal property.

In this research, we will further describe the benefits of wavelet phase reconstruction. The wavelet technique offers a computational efficiency of $O(n)$ using finite impulse

response filters. Hampton's derivation uses the Haar wavelet and then either uses a Poisson smoother or recommends a denoiser as a follow-up step [22]. Our derivation in this paper is made to be robust to noise using wavelets that have a longer basis length, yielding a smoother reconstruction without a follow-up step. Using noise-free data, the approach also yields an exact reconstruction with a zero mean of the 2D data. We also extend Hampton's work to provide for a solution that requires no boundary conditions for the Haar wavelet on a square aperture where the side dimensions are a power of 2.

While most ground-based AO systems can be built with appropriate computational power, space-based AO systems have to work within the available size, weight, and power requirements of a flight-certified processor. Increasing the actuator or sensor densities will quickly consume the available resources using the traditional approaches. By applying signal processing concepts to this problem, we are able to reduce the processing requirements.

The wavelet approach is based on a multiresolution analysis solution type. As a consequence of how the DWT is employed, the grid size must be a power of 2. In a Cartesian coordinate frame, wavefront values are reconstructed first on a 2×2 grid, then 4×4, then 8×8, and expands by a power of 2 in size for each iteration. Iteration in this context means that the matrix dimension of processed data is doubled each time, not that the full data are processed repeatedly. However, there is no preconditioner or approximation required. The solution algorithm constructs the data for each iteration entirely using the slope measurements provided from the Shack–Hartmann wavefront sensor.

The outline of this paper is as follows. Section 2 details the necessary signal processing theory to explain the notation and how wavelets are related to wavefront reconstruction. Section 3 derives the wavefront reconstruction algorithm for the first two iterations. Section 4 derives additional steps to improve performance for data from a telescope with obscurations. Section 5 provides some discussion and simulated wavefront reconstruction examples for several cases. We provide concluding remarks in Section 6 and further math details in Appendix A.

2. THEORETICAL FRAMEWORK

A. Two-Dimensional Signal Processing

The derivation for wavelet phase reconstruction requires some building blocks from multidimensional signal processing. We begin by defining a 2D sequence, $x[n_1, n_2]$, which is a known quantity at each lattice point $[n_1, n_2]$. We define the lattice to be finite in extent and have dimension lengths of powers of 2, usually of the form $2^N \times 2^N$.

We define two unit-shift operators, z_1 and z_2, where the subscript denotes either the n_1 or n_2 direction. These definitions arise from the 2D Z-transform

$$X(z_1, z_2) = \sum_{n_1=-\infty}^{\infty} \sum_{n_2=-\infty}^{\infty} x[n_1, n_2] z_1^{-n_1} z_2^{-n_2}. \tag{1}$$

A 2D filter $H(z_1, z_2)$ is separable if it can be factored as two functions of a single variable, as in $H(z_1, z_2) = H_1(z_1)H_2(z_2)$. To express the 2D filtering convolution [23], we can write

$$y = H(z_1, z_2)x[n_1, n_2] = H_1(z_1)H_2(z_2)x \tag{2}$$

To simplify notation, we use operator notation and disregard the indices. Equation (2) is written with the sequence on the right side as the operand. When multiple operators are written, they are performed from right to left starting from the operand. The presence of a filter in operator notation implies the convolution operation (traditionally expressed as $h * *x$ for 2D convolution). Since the filter is separable, we observe that $H_1(z_1)H_2(z_2)x = H_2(z_2)H_1(z_1)x$ and that the order of operation does not change the final result.

The algorithm proposed here is performed on a multigrid, and it is multiresolution [24]. To move between the resampled lattices, the downsample and upsample operators are used. We define downsampling by a factor of 2 as

$$\begin{aligned} y_1 &= D_1 x \Leftrightarrow y_1[n_1, n_2] = x[2n_1, n_2], \\ y_2 &= D_2 x \Leftrightarrow y_2[n_1, n_2] = x[n_1, 2n_2], \\ y_3 &= D_1 D_2 x = D_2 D_1 x \Leftrightarrow y_3[n_1, n_2] = x[2n_1, 2n_2]. \end{aligned} \tag{3}$$

The downsampling operator discards the odd-index entries for the downsampling phase of 0 and discards the even-index entries for the downsampling phase of 1, the latter of which is not shown in Eq. (3). This concept will be further explored later in Section 5.B.

Likewise, the upsampling operator can be defined as

$$\begin{aligned} y_1 = U_1 x \Leftrightarrow \begin{cases} y_1[2n_1, n_2] = x[n_1, n_2] \\ y_1[2n_1 + 1, n_2] = 0 \end{cases}, \\ y_2 = U_2 x \Leftrightarrow \begin{cases} y_2[n_1, 2n_2] = x[n_1, n_2] \\ y_2[n_1, 2n_2 + 1] = 0 \end{cases} \end{aligned} \tag{4}$$

for each dimension. Equation (4) shows the relationship for upsampling phase 0; swap the $x[n_1, n_2]$ and 0 to show upsampling phase 1.

Equation (4) is also separable, and the relationship $y = U_1 U_2 x = U_2 U_1 x$ shows that the order of operations can be swapped. Although downsampling and upsampling by any positive integer factor is possible, this algorithm only uses a factor of 2. Thus, both operator forms do not show the resampling factor, only the dimension in which the operator performs.

Separable filters have useful properties to simplify implementation by dealing with only one dimension at a time. However, when a serial grouping of operators perform in the same dimension, in general the order of operations cannot be changed arbitrarily. This restriction is shown in Fig. 1. We must use the Noble identities to correctly establish the relationship in instances such as

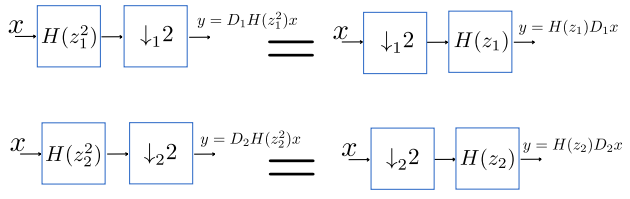

Fig. 1. Noble identities in a block diagram showing the equivalency of Eq. (5) for both dimensions. The serial combination of two operations that both occur in the same dimension cannot change order without changing the filtering operation.

$$y_1 = D_1 H(z_1^2)x = H(z_1)D_1 x,$$
$$y_2 = D_2 H(z_2^2)x = H(z_2)D_2 x. \tag{5}$$

B. Tree Structure and Two-Dimensional Quadrature Mirror Filters

A tree structure is a signal processing technique to decompose a single-dimensional signal, $x[n]$, into multiple channels. In the case of this algorithm, each branch has two channels. In multirate systems, the channels are usually a low- and high-pass filters.

A special circumstance of the tree structure is referred as a quadrature mirror filter (QMF), shown in Fig. 2. It is composed of four filters, two used for analysis (with tildes) and two used for synthesis (without tildes). We can express the output as a function of the input using

$$y = (G(z)UD\tilde{G}(z) + H(z)UD\tilde{H}(z))x. \tag{6}$$

The filters that are used in a QMF system are specifically designed in a manner to cancel out aliasing effects due to non-ideal frequency response of the filters such that

$$G(z)UD\tilde{G}(z) + H(z)UD\tilde{H}(z) = z^{-L}, \tag{7}$$

which means that the output y is a perfect reconstruction of x shifted by L. The perfect reconstruction property of the filters is explained in detail in [25]. The shift can be thought of as a processing delay of the filters.

The channels can be named "approximation" and "details" based on the approximation looking similar to the original signal at a lower sampling rate and the details providing information of how the approximation differs from the higher resolution signal. The DWT takes the original sequence and creates the approximation and details sequences. The inverse transform performs the opposite. Apart from a few exceptions, it turns out that the approximation contains more Shannon entropy than the details [26].

In the case of a multidimensional signal, we can decompose in each dimension independently. In the case of a 2D signal, this becomes a two-level implementation with four output channels.

The four output channels can be described similar to the QMF terminology, where x_{LL} is the approximation and x_{LH}, x_{HL}, and x_{HH} are the details. Figure 3 depicts the 2D DWT. Here the approximation also maintains more Shannon entropy than the details. This will be discussed further in Section 5.A.

Likewise, if the four channels are known, we can perform the 2D inverse DWT to perfectly reconstruct the original 2D sequence.

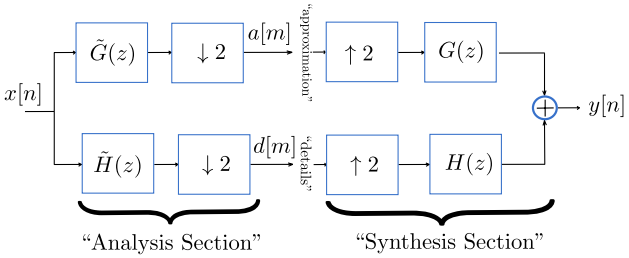

Fig. 2. Tree structure of a QMF for a single dimensional signal $x[n]$. Tree structures with the perfect reconstruction property result in $y[n]$ being equivalent to a shifted $x[n]$. The channel with $\tilde{G}(z)$ is a low-pass filter, and the channel with $\tilde{H}(z)$ is a high-pass filter.

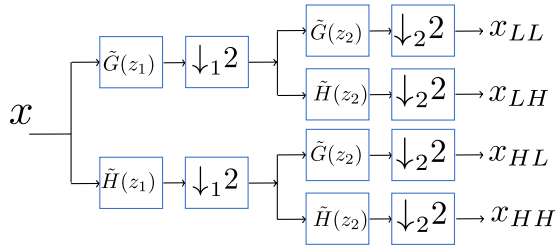

Fig. 3. Two-dimensional QMF for the analysis section.

C. Wavelets in Tree Structure and Factoring Wavelets

In engineering applications, reference to wavelets implies the presence of both low- and high-pass filters. There are many classes of wavelets based on their inherent properties including orthogonal, vanishing moments, and others. The proposed algorithm relies on the orthogonal property, which means the Haar, Daubechies, and biorthogonal families of wavelets can be used.

The Haar wavelet is the most simple and was originally introduced in 1909 [27]. The Haar low- and high-pass filters are defined as

$$g(z) \triangleq \frac{1}{\sqrt{2}}(1 + z^{-1}), \qquad g(-z) \triangleq \frac{1}{\sqrt{2}}(1 - z^{-1}). \tag{8}$$

The coefficient of the Haar wavelet is to ensure that the output is normalized with respect to the input. The Haar high-pass filter has a nice property:

$$g(-z^N) = \left(\sum_{\ell=0}^{N-1} z^{-\ell}\right) g(-z) \quad \forall\, N \geq 1$$
$$= \left(\sum_{\ell=0}^{\frac{N}{2}-1} z^{-2\ell}\right) \sqrt{2}g(z)g(-z) \quad \text{if } N \text{ is even}, \tag{9}$$

which will be needed later to simplify expressions. The first expression is used when a high-pass filter is needed; the second expression is used when a low-pass filter is needed. Equation (9) reveals that high-order complexity filters can be implemented as a delayed summation of first-order filters. Its complete proof is shown in Appendix A.

The filters associated with the orthogonal wavelet families can be factored as follows:

$$G(z) = g(z)G_0(z), \qquad H(z) = g(-z)H_0(z),$$
$$\tilde{G}(z) = g(z)\tilde{G}_0(z), \qquad \tilde{H}(z) = g(-z)\tilde{H}_0(z). \tag{10}$$

In the particular case of the Haar wavelet, the factoring can be $G_0(z) = H_0(z) = \tilde{G}_0(z) = 1$; $\tilde{H}_0(z) = -1$. The factoring of Eq. (10) makes phase reconstruction possible for wavelet families with the orthogonal property.

D. Relationship of Wavelets to Shack–Hartmann Measurements

The Fried model of a Shack–Hartmann sensor [5] is shown in Fig. 4. The model defines the relationship between slope measurements and phase point values as

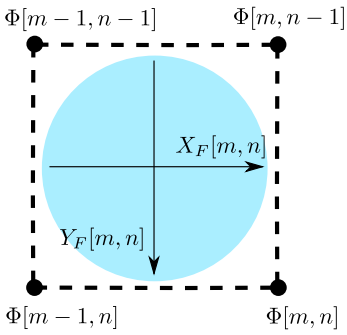

Fig. 4. Fried geometry relationship between phase points and their measured slope lattice for a single lenslet. A Shack–Hartmann sensor will have an array of these lenslets.

$$\begin{aligned} X_F[m,n] &= \frac{1}{2}(\Phi[m,n-1]-\Phi[m-1,n-1] \\ &\quad +\Phi[m,n]-\Phi[m-1,n]), \\ Y_F[m,n] &= \frac{1}{2}(\Phi[m-1,n]-\Phi[m-1,n-1] \\ &\quad +\Phi[m,n]-\Phi[m,n-1]). \end{aligned} \tag{11}$$

Equation (11) was rewritten from its original form in [5] to appear in causal form. As a result, close observation of Eq. (11) reveals that the slope measurements can be written as a separable filtering operation on the phase points. It involves one low-pass filter and one high-pass filter and is stated in operator form as

$$\begin{aligned} X_F &= g(-z_2)g(z_1)\Phi, \\ Y_F &= g(-z_1)g(z_2)\Phi. \end{aligned} \tag{12}$$

The relationship of Eq. (12) is the connection of the Haar wavelet to the Fried geometry; X_F and Y_F are the slope measurements. Figure 5 depicts the block diagram relationship of the Hudgin [6] and Fried geometries to the wavefront. However, as we will see in Section 3.A, there is not a direct solution to solve for Φ based on these equations. In order to reconstruct Φ from the slope measurements, the tree structure 2D QMF is employed. We are then able to specify some additional information to reconstruct the wavefront.

3. PHASE RECONSTRUCTION ALGORITHM

A. Iteration for Level 1

From observation of the 2D QMF in Fig. 3, we can write equations that relate the phase points to the four channels of the 2D QMF as

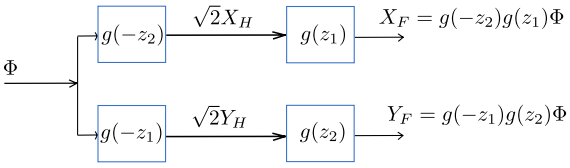

Fig. 5. Block diagram relationship between the phase points and the Hudgin and Fried geometries.

$$\begin{aligned} \phi^1_{LL} &= D_2D_1\tilde{G}(z_2)\tilde{G}(z_1)\Phi, \\ \phi^1_{LH} &= D_2D_1\tilde{H}(z_2)\tilde{G}(z_1)\Phi, \\ \phi^1_{HL} &= D_2D_1\tilde{G}(z_2)\tilde{H}(z_1)\Phi, \\ \phi^1_{HH} &= D_2D_1\tilde{H}(z_2)\tilde{H}(z_1)\Phi. \end{aligned} \tag{13}$$

We have swapped the order of the operators in Eq. (13) for a convenience of notation and use the superscript 1 to denote the first iteration, not an exponent. Using the factoring of Eq. (10) in Eq. (13), we can make the following substitutions:

$$\begin{aligned} \phi^1_{LH} &= D_2D_1\tilde{H}_0(z_2)\tilde{G}_0(z_1)(g(-z_2)g(z_1)\Phi) \\ &= D_2D_1\tilde{H}_0(z_2)\tilde{G}_0(z_1)X_F, \\ \phi^1_{HL} &= D_2D_1\tilde{G}_0(z_2)\tilde{H}_0(z_1)(g(z_2)g(-z_1)\Phi) \\ &= D_2D_1\tilde{G}_0(z_2)\tilde{H}_0(z_1)Y_F. \end{aligned} \tag{14}$$

The remaining two quantities, ϕ^1_{LL} and ϕ^1_{HH}, do not have a simple relationship to the slope measurements X_F and Y_F, because the filters of Eq. (13) are both low pass or high pass, whereas the slope definitions require one of each.

If they did have a trivial relationship, then reconstruction would be a simple 2D inverse DWT transform. We need to further explore ϕ^1_{LL} and ϕ^1_{HH} in order to determine if such a reconstruction is possible.

B. Iteration for Level 2

In this algorithm, when there is an unknown quantity, we apply the 2D DWT and break apart the unknown quantity into 4 new channels. We now explore the second iteration to determine if any further substitution of Φ is possible with known slope measurements. Because we have two unknown quantities, we must do this for both the ϕ^1_{LL} and ϕ^1_{HH} channels. First we will only consider ϕ^1_{LL}; we start by writing out the expressions for the four channels in the analysis:

$$\begin{aligned} \phi^2_{LL/L} &= D_2D_1\tilde{G}(z_2)\tilde{G}(z_1)\phi^1_{LL} \\ &= D_2D_1\tilde{G}(z_2)\tilde{G}(z_1)D_2D_1\tilde{G}(z_2)\tilde{G}(z_1)\Phi, \\ \phi^2_{LH/L} &= D_2D_1\tilde{H}(z_2)\tilde{G}(z_1)\phi^1_{LL} \\ &= D_2D_1\tilde{H}(z_2)\tilde{G}(z_1)D_2D_1\tilde{G}(z_2)\tilde{G}(z_1)\Phi, \\ \phi^2_{HL/L} &= D_2D_1\tilde{G}(z_2)\tilde{H}(z_1)\phi^1_{LL} \\ &= D_2D_1\tilde{G}(z_2)\tilde{H}(z_1)D_2D_1\tilde{G}(z_2)\tilde{G}(z_1)\Phi, \\ \phi^2_{HH/L} &= D_2D_1\tilde{H}(z_2)\tilde{H}(z_1)\phi^1_{LL} \\ &= D_2D_1\tilde{H}(z_2)\tilde{H}(z_1)D_2D_1\tilde{G}(z_2)\tilde{G}(z_1)\Phi. \end{aligned} \tag{15}$$

We are using the superscript 2 for the second iteration and add the $/L$ subscript for the ϕ^1_{LL} data. There is additionally a $/H$ analysis for the ϕ^1_{HH} data. For brevity, we will only state the HH results at the end of this section, since their development follows the same analysis, but we emphasize that the resulting expression is not exactly the same. Examining Eq. (15) reveals that while $\phi^2_{LL/L}$ is only composed of low-pass filters, the remaining three channels have a combination of low- and high-pass filters. If we factor the filters as in Eq. (10), we will again find substitutions with the measured slope data. For $\phi^2_{LH/L}$ we obtain

$$\begin{aligned}\phi^2_{LH/L} &= D_2D_1\tilde{H}_0(z_2)g(-z_2)\tilde{G}(z_1)D_2D_1\tilde{G}(z_2)\tilde{G}_0(z_1)g(z_1)\Phi \\ &= D_2D_1\tilde{H}_0(z_2)\tilde{G}(z_1)D_2D_1\tilde{G}(z_2)\tilde{G}_0(z_1)(g(-z_2^2)g(z_1)\Phi) \\ &= D_2D_1\tilde{H}_0(z_2)\tilde{G}(z_1)D_2D_1\tilde{G}(z_2)\tilde{G}_0(z_1)g(z_2)\left(\sqrt{2}X_F\right).\end{aligned} \tag{16}$$

where the final step uses the high-pass filter simplification of Eq. (9). Using the same procedure, we can also solve for $\phi^2_{HL/L}$ as

$$\begin{aligned}\phi^2_{HL/L} &= D_2D_1\tilde{G}(z_2)\tilde{H}_0(z_1)g(-z_1)D_2D_1\tilde{G}_0(z_2)g(z_2)\tilde{G}(z_1)\Phi \\ &= D_2D_1\tilde{G}(z_2)\tilde{H}_0(z_1)D_2D_1\tilde{G}_0(z_2)\tilde{G}(z_1)(g(-z_1^2)g(z_2)\Phi) \\ &= D_2D_1\tilde{G}(z_2)\tilde{H}_0(z_1)D_2D_1\tilde{G}_0(z_2)\tilde{G}(z_1)g(z_1)\left(\sqrt{2}Y_F\right).\end{aligned} \tag{17}$$

The final channel, $\phi^2_{HH/L}$, yields two possible simplifications:

$$\begin{aligned}\phi^2_{HH/L} &= D_2D_1\tilde{H}_0(z_2)g(-z_2)\tilde{H}(z_1)D_2D_1\tilde{G}(z_2)\tilde{G}_0(z_1)g(z_1)\Phi \\ &= D_2D_1\tilde{H}_0(z_2)\tilde{H}(z_1)D_2D_1\tilde{G}(z_2)\tilde{G}_0(z_1)(g(-z_2^2)g(z_1)\Phi)\end{aligned} \tag{18}$$

or, similarly,

$$= D_2D_1\tilde{H}_0(z_1)\tilde{H}(z_2)D_2D_1\tilde{G}(z_2)\tilde{G}_0(z_1)(g(-z_1^2)g(z_2)\Phi).$$

The two possible substitutions arise from the flexibility of having two high-pass filters. Either simplification is exact when using noise-free data. Rather than choosing one definition over the other, we take an average:

$$\begin{aligned}\phi^2_{HH/L} = &\frac{1}{2}D_2D_1\tilde{H}_0(z_2)\tilde{H}(z_1)D_2D_1\tilde{G}(z_2)\tilde{G}_0(z_1)g(z_2)\left(\sqrt{2}X_F\right) \\ &+\frac{1}{2}D_2D_1\tilde{H}(z_2)\tilde{H}_0(z_1)D_2D_1\tilde{G}_0(z_2)\tilde{G}(z_1)g(z_1)\left(\sqrt{2}Y_F\right).\end{aligned} \tag{19}$$

The averaging of Eq. (19) allows for some robustness to noise in the slope measurements at very little computational cost. The $1/2$ coefficient simply assumes additive white Gaussian noise. Correlation statistics analysis may provide a better coefficient. Using the same process for the HH data, we now state the results as

$$\begin{aligned}\phi^2_{LH/H} &= D_2D_1\tilde{H}_0(z_2)\tilde{G}(z_1)D_2D_1\tilde{H}(z_2)\tilde{H}_0(z_1)g(-z_2)\left(\sqrt{2}Y_F\right), \\ \phi^2_{HL/H} &= D_2D_1\tilde{G}(z_2)\tilde{H}_0(z_1)D_2D_1\tilde{H}(z_1)\tilde{H}_0(z_2)g(-z_1)\left(\sqrt{2}X_F\right), \\ \phi^2_{HH/H} = &\frac{1}{2}D_2D_1\tilde{H}_0(z_2)\tilde{H}(z_1)D_2D_1\tilde{H}(z_2)\tilde{H}_0(z_1)g(-z_2)\left(\sqrt{2}Y_F\right) \\ &+\frac{1}{2}D_2D_1\tilde{H}(z_2)\tilde{H}_0(z_1) \\ &\ldots D_2D_1\tilde{H}_0(z_2)\tilde{H}(z_1)g(-z_1)\left(\sqrt{2}X_F\right).\end{aligned} \tag{20}$$

We have now completed the derivation of the second iteration and show it in Fig. 6. While the equations look complex on paper, actual implementations are straightforward and efficient in processing performance. Every expression is simply a serial grouping of the filter-filter-downsample-downsample block.

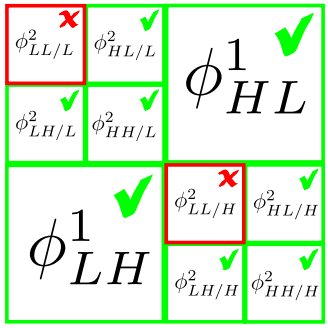

Fig. 6. 2D QMF diagram of the channels at the second iteration. The upper left and lower right are each divided into four channels.

C. Further Iterations

We are able to generalize the formulation for additional iterations and include the necessary information in Section 2 of Appendix A.

By developing this level of k implementation, we are able to scale the algorithm for any power-of-2-sized data quickly. This algorithm is possible due to the flexibility of the high-pass filter combined with the simplification of Eq. (9); hence, the nomenclature wavelet phase reconstruction is appropriate. Due to these features, we are able to swap out definitions of channels with Φ using the known, measured quantities X_F and Y_F.

D. Setting the Mean and Waffle Values

At the final iteration, we have two sets of 2×2 matrices and no further downsampling is required. The upper-left scalar value of each is significant and represents the ϕ_{LL} channel that has gone undetermined for all prior iterations. Each value represents undetected modes of the Fried geometry: the piston and waffle modes. The piston represents the mean of the entire Φ data set. Since the Shack–Hartmann sensor only measures differences between phase points and not absolute values, the mean value cannot be known. We can assign it a value of zero and accept that we are within a constant value of the actual piston of the wavefront. A separate sensor is required for measuring the piston. The waffle mode represents a nuisance checkerboard pattern along the phase points with a mean of zero. We show the completed 2D QMF analysis section structure in Fig. 7, where all values are known.

E. Synthesis Section

Up until this section, all of the previous algorithm code has been used to iteratively create the four-channel blocks of the analysis section. We separated each unknown channel into four subchannels. While we did not have the direct information for each channel, we were able to substitute for it using the measurements that were available. The analysis section is now complete and must now take the four channel blocks and perform the inverse DWT, as shown in Fig. 8. In doing so, we recreate the unknown channel of the previous iteration. We recursively perform this until we have no more four-channel blocks, which is the final solution of the wavefront phase surface.

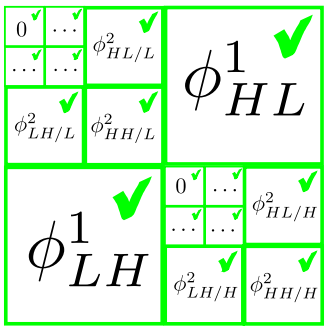

Fig. 7. 2D QMF performed iteratively on the upper left and lower right until scalar values remain.

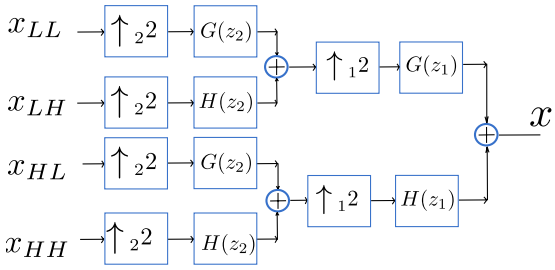

Fig. 8. Synthesis section of the 2D QMF.

F. Implementation Efficiency

This wavefront reconstruction algorithm can be split across multiple processors. The channel definitions use information that was calculated in the previous iterations or shared at the same iteration. The common operations can be seen in Eq. (20). In most cases of the algorithm, the $\sqrt{2}$ multiplications in the derivation come in pairs, which can be handled as a trivial binary shift operation.

The quantity of multiplications to determine all ϕ channels is approximately upper bounded by $O(10(\mathrm{FL})^2 n/3)$, where FL is the filter length, which for approximation purposes we take to be the max of the filter lengths for $\tilde{G}(z)$, $\tilde{G}_0(z)$, $\tilde{H}(z)$, and $\tilde{H}_0(z)$. Filter lengths are explained in further detail in Section 5.C. Determining Φ requires $O(20(\mathrm{FL})^2 n/3)$ multiplications. Thus, a Daubechies 6 filter reconstruction is comparable to other algorithms in computational requirement.

4. TELESCOPE APERTURES

The wavefront reconstruction algorithm presented in Section 3 can be directly applied to data from a telescope with a nonsquare aperture and other features such as a segmented primary mirror and central obscurations from the secondary mirror and support structure. There will, however, be errors near the boundary edges where the Fried model is incorrect. For improved performance, this section explains how to correct for errors at the boundary for masked data stored within a $2^N \times 2^N$ matrix. However, this improvement is costly computationally compared to the original algorithm. The results presented here are a full theoretical explanation, and reductions in operations would be used in an actual real-time implementation. We begin by defining the mask, or window function, as

$$w[\underline{n}] = \begin{cases} 0 & \text{outside aperture} \\ 1 & \text{inside aperture} \end{cases}, \tag{21}$$

where we use notation $\underline{n} = n_1, n_2$ to simplify the expressions. We define the Fried gradient operator as

$$\nabla_F(\underline{z}) = \begin{bmatrix} g(z_1)g(-z_2) \\ g(-z_1)g(z_2) \end{bmatrix}, \tag{22}$$

which calculates the values X_F and Y_F for Eq. (12).

With these two definitions, we can now define two sets of indices for the boundary and inside the aperture as

$$\begin{aligned} \mathcal{B} &= \{\underline{n} \,|\, \|\nabla_F w[\underline{n}]\| \neq 0\}, \\ \mathcal{W} &= \{\underline{n} \,|\, \|\nabla_F w[\underline{n}]\| = 0 \quad \text{and} \quad w[\underline{n}] = 1\}. \end{aligned} \tag{23}$$

The reconstruction algorithm presented in Section 3 using the Haar wavelet is expressed as an operator $\mathcal{H}$ such that

$$\Phi[\underline{n}] = \mathcal{H}(\nabla_F \Phi[\underline{n}]) \tag{24}$$

provided the mean and waffle modes are both zero. Since phase reconstruction involves only linear operators, it is linear. By having this property, we can then write the expression

$$\begin{aligned} \nabla_F(w[\underline{n}]\Phi[\underline{n}]) &= w[\underline{n}]\nabla_F\Phi[\underline{n}] + [\nabla_F(w[\underline{n}]\Phi[\underline{n}]) - w[\underline{n}]\nabla_F\Phi[\underline{n}]] \\ &= w[\underline{n}]\begin{bmatrix} X_F[\underline{n}] \\ Y_F[\underline{n}] \end{bmatrix} + E[\underline{n}], \end{aligned} \tag{25}$$

where we define the error, $E[\underline{n}]$, to be the quantity in square brackets. Since it can be easily seen that $E[\underline{n}]$ is identically zero outside the boundary, as

$$E[\underline{n}] = 0 \Leftrightarrow \underline{n} \notin \mathcal{B}, \tag{26}$$

the error can be written as

$$E[\underline{n}] = \sum_{\underline{\ell} \in \mathcal{B}} \begin{bmatrix} \tilde{X}_{\underline{\ell}} \\ \tilde{Y}_{\underline{\ell}} \end{bmatrix} \delta[\underline{n} - \underline{\ell}], \tag{27}$$

where $\delta[\underline{n}]$ is the 2D Kronecker delta function. The quantities $\tilde{X}_{\underline{\ell}}$ and $\tilde{Y}_{\underline{\ell}}$ are the incorrect slope boundaries that contribute to the error. Solving for these values allows their contribution to the error to be canceled.

We can solve for $\tilde{X}_{\underline{\ell}}$ and $\tilde{Y}_{\underline{\ell}}$ by performing the Haar reconstruction operator to both sides of Eq. (25), which results in

$$\begin{aligned} w[\underline{n}]\Phi[\underline{n}] = \mathcal{H}\left(w[\underline{n}]\begin{bmatrix} X_F[\underline{n}] \\ Y_F[\underline{n}] \end{bmatrix}\right) &+ \sum_{\underline{\ell} \in \mathcal{B}} \tilde{X}_{\underline{\ell}} \mathcal{H}\left(\begin{bmatrix} \delta[\underline{n} - \underline{\ell}] \\ 0 \end{bmatrix}\right) \\ &+ \sum_{\underline{\ell} \in \mathcal{B}} \tilde{Y}_{\underline{\ell}} \mathcal{H}\left(\begin{bmatrix} 0 \\ \delta[\underline{n} - \underline{\ell}] \end{bmatrix}\right) \quad \forall\, \underline{n}. \end{aligned} \tag{28}$$

By taking the Fried gradient operator of both sides of Eq. (28), we obtain, for $\underline{n} \in \mathcal{W}$,

$$\begin{bmatrix} X_F[\underline{n}] \\ Y_F[\underline{n}] \end{bmatrix} = \nabla_F \mathcal{H}\left(w[\underline{n}]\begin{bmatrix} X_F[\underline{n}] \\ Y_F[\underline{n}] \end{bmatrix}\right) + \sum_{\underline{\ell} \in \mathcal{B}} \mathbf{\Gamma}_X \tilde{X}_{\underline{\ell}} + \sum_{\underline{\ell} \in \mathcal{B}} \mathbf{\Gamma}_Y \tilde{Y}_{\underline{\ell}}. \tag{29}$$

Using linearity, we define the impulse responses:

$$\mathbf{\Gamma}_X[\underline{n},\underline{\ell}] = \nabla_F\mathcal{H}\left(\begin{bmatrix}\delta[\underline{n}-\underline{\ell}]\\ 0\end{bmatrix}\right) \in \mathbb{R}^{2\times 1},$$
$$\mathbf{\Gamma}_Y[\underline{n},\underline{\ell}] = \nabla_F\mathcal{H}\left(\begin{bmatrix}0\\ \delta[\underline{n}-\underline{\ell}]\end{bmatrix}\right) \in \mathbb{R}^{2\times 1} \tag{30}$$

for $\underline{n}\in\mathcal{W}$, $\underline{\ell}\in\mathcal{B}$. These definitions can be precomputed and have no dependence on the slope measurements.

Using the impulse responses $\mathbf{\Gamma}_X[\underline{n},\underline{\ell}]$ and $\mathbf{\Gamma}_Y[\underline{n},\underline{\ell}]$ for $\underline{n}\in\mathcal{W}$ and $\underline{\ell}\in\mathcal{B}$, we can solve for $\tilde{X}_{\underline{\ell}}$ and $\tilde{Y}_{\underline{\ell}}$ in Eq. (28) from a set of linear equations as

$$\begin{bmatrix}X_F[\underline{n}]\\ Y_F[\underline{n}]\end{bmatrix} - \nabla_F\mathcal{H}\left(w[\underline{n}]\begin{bmatrix}X_F[\underline{n}]\\ Y_F[\underline{n}]\end{bmatrix}\right) = \sum_{\underline{\ell}\in\mathcal{B}}\mathbf{\Gamma}_X[\underline{n},\underline{\ell}]\tilde{X}_{\underline{\ell}} + \sum_{\underline{\ell}\in\mathcal{B}}\mathbf{\Gamma}_Y[\underline{n},\underline{\ell}]\tilde{Y}_{\underline{\ell}} \tag{31}$$

for $\underline{n}\in\mathcal{W}$. The left-hand side is known from the measured gradients, and Eq. (31) yields $n_{\mathcal{W}} = 2|\mathcal{W}|$ equations in $n_{\mathcal{B}} = 2|\mathcal{B}|$ unknowns, with $|\mathcal{W}|$ and $|\mathcal{B}|$ the number of sample points inside the aperture and on the boundary, respectively. It can easily be seen that Eq. (31) can be written in matrix form as

$$\underline{z}_{\mathcal{W}} = \mathbf{\Gamma}\underline{\tilde{z}}_{\mathcal{B}}, \tag{32}$$

where $\underline{z}_{\mathcal{W}}$ and $\underline{\tilde{z}}_{\mathcal{B}}$ are the corresponding $n_{\mathcal{W}}\times 1$ and $n_{\mathcal{B}}\times 1$ vectors on the left- and right-hand sides of Eq. (31) and $\mathbf{\Gamma}$ is the corresponding $n_{\mathcal{W}}\times n_{\mathcal{B}}$ matrix. Equation (32) is underdetermined and therefore is a least-squares solution. The solution for $\underline{\tilde{z}}_{\mathcal{B}} = (\mathbf{\Gamma}^T\mathbf{\Gamma})^{-1}\mathbf{\Gamma}^T\underline{z}_{\mathcal{W}}$ can be reduced in operations due to many zero-value eigenvalues.

To give an idea of the dimensionality, for a 64×64 data matrix containing a circular aperture with radius $\rho = 29$, the matrix $\mathbf{\Gamma}\in\mathbb{R}^{4976\times 456}$. However, since all gradients on the boundary yield redundant information, it turns out that the number of unknowns can be considerably reduced. In this example, the matrix $\mathbf{\Gamma}^T\mathbf{\Gamma}$ can be decomposed as

$$\mathbf{\Gamma}^T\mathbf{\Gamma} = \mathbf{U}\Lambda\mathbf{U}^T, \tag{33}$$

where $\lambda_i = \mathrm{diag}(\Lambda)$ are the eigenvalues as shown in Fig. 9. The first 283 eigenvalues are zero, and only $M = 173$ eigenvalues are not zero. As a consequence, we can factor

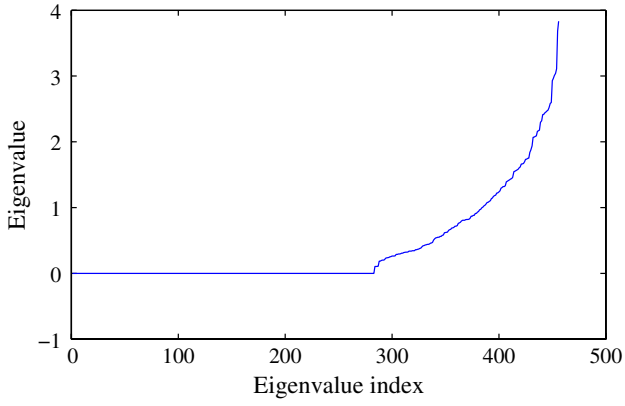

Fig. 9. Eigenvalues of the 64×64 circular aperture in monotonic order.

$$\mathbf{\Gamma}^T\mathbf{\Gamma} = \bar{\mathbf{U}}\,\bar{\Lambda}\,\bar{\mathbf{U}}^T, \tag{34}$$

with $\bar{\Lambda} = \mathrm{diag}(\lambda_1,\ldots,\lambda_M)$, $\lambda_i > 0$ and $\bar{\mathbf{U}}\in\mathbb{R}^{n_{\mathcal{B}}\times M}$ orthonormal. Based on this decomposition, the corrective term $\underline{z}_{\mathcal{B}}$ can be solved as

$$\underline{\alpha} = \bar{\Lambda}^{-1}\bar{\mathbf{U}}^T\bar{\mathbf{\Gamma}}^T\underline{z}_{\mathcal{W}}, \underline{\tilde{z}}_{\mathcal{B}} = \bar{\mathbf{U}}\,\underline{\alpha}, \tag{35}$$

where the matrices $\bar{\Lambda}^{-1}\bar{\mathbf{U}}^T\bar{\mathbf{\Gamma}}^T$ and $\bar{\mathbf{U}}$ are $M\times n_{\mathcal{W}}$ and $n_{\mathcal{B}}\times M$, respectively. In the example, they would be 173×4976 and 456×173, respectively.

Having solved for $\underline{\tilde{z}}_{\mathcal{B}}$, we now can use $\tilde{X}_{\underline{\ell}}$ and $\tilde{Y}_{\underline{\ell}}$ in Eq. (31), so that we have the corrected gradients of $w[\underline{n}]\bar{\Phi}[\underline{n}]$ as

$$X[\underline{n}] = X_F[\underline{n}] + \sum_{\underline{\ell}\in\mathcal{B}}\tilde{X}_{\underline{\ell}}\delta[\underline{n}-\underline{\ell}], Y[\underline{n}] = Y_F[\underline{n}] + \sum_{\underline{\ell}\in\mathcal{B}}\tilde{Y}_{\underline{\ell}}\delta[\underline{n}-\underline{\ell}]. \tag{36}$$

Using the corrected gradients X and Y, the wavefront reconstruction algorithm is then run (with the option of a different wavelet for better results) to obtain the wavefront phase estimate.

5. DISCUSSION

A. Discarding the HH Channel

Under light turbulence assumptions, the HH channel should be very small and contain little energy that is needed for reconstruction. Another way of stating this is that since the Shannon entropy is low, it contains little information about the nature of the wavefront. If computational constraints exist to meet feedback control bandwidth requirements, the entire HH channel can be disregarded and set to zero. The result then becomes an approximation of the actual wavefront.

B. Resampling Phase Effects on the Boundary Conditions

As discussed a number of times, the choice of wavelets has an effect on the phase reconstruction and its sensitivity to noise. Higher-order wavelets (such as the Daubechies family) yield filters with longer impulse response and better filtering capabilities.

The drawback of filters with longer impulse response is clearly the fact that their responses have longer transients and they are affected by boundary conditions. Wavelet filters are specifically designed to cancel aliasing effects that arise from having nonideal filters ($G(z)$ and $\tilde{G}(z)$ are not ideal low-pass filters, and $H(z)$ and $\tilde{H}(z)$ are not ideal high-pass filters). While the convolution operation is still close to the boundary, this aliasing cancellation effect has not fully initialized, and this is also known as the transient region (because the wavelets are not operating as designed). Thus, the output of reconstruction in this region is unreliable.

On the other hand, the Haar wavelet, which yields the simplest first-order filters at all the stages, if properly implemented, is completely independent of the boundary conditions, provided the data matrix is square with dimensions as a power of 2.

This can be obtained by adding a positive shift at the analysis network (see Fig. 2), so that the four filters become

$$\tilde{G}(z) = zg(z), \qquad \tilde{H}(z) = zg(-z),$$
$$G(z) = g(z), \qquad H(z) = -g(-z), \tag{37}$$

using $g(z)$ defined in Eq. (8). With this choice of filters, the "approximation" and "details" signals $a[m]$ and $d[m]$ in Fig. 2 can be related to the input $x[n]$ as

$$a[m] = \frac{1}{\sqrt{2}}(x[2m+1] + x[2m]),$$
$$d[m] = \frac{1}{\sqrt{2}}(x[2m+1] - x[2m]), \tag{38}$$

and the output becomes

$$y[2m] = \frac{1}{\sqrt{2}}(a[m] - d[m]) = x[2m],$$
$$y[2m+1] = \frac{1}{\sqrt{2}}(a[m] + d[m]) = x[2m+1]. \tag{39}$$

This yields perfect reconstruction $y[n] = x[n],\ n = 0, \ldots, N-1$, provided the data length N is even, regardless of boundary conditions. In other words, in the case of the Haar wavelet, the effects of boundary conditions get discarded by the resampling operations.

If the data length is a power of 2, this will be true for all resolution levels in the decomposition.

C. Effects of Filter Selection on Noise

The major contribution of this work, compared to Hampton's derivation [20], is the availability of the factored polynomials $G_0(z)$ and $H_0(z)$. The Fried model is not always an accurate reconstruction of the wavefront, since it only relates neighboring sample points, as seen in Eq. (11). Some have suggested other reconstruction polynomials such as a Taylor series, since they have a longer basis and therefore have a smoothing property.

The Daubechies family filters are numbered starting at 1 (which is the Haar wavelet), and each number corresponds to different filter lengths (or equivalently polynomial lengths). The number of filter coefficients in $\tilde{G}(z)$, $\tilde{H}(z)$, $G(z)$, and $H(z)$ are all twice the Daubechies number. For example, Daubechies 3 uses filters of length 6.

The factored coefficients of the filters are shown in Figs. 10 and 11. Each filter is centered when being applied, due to the

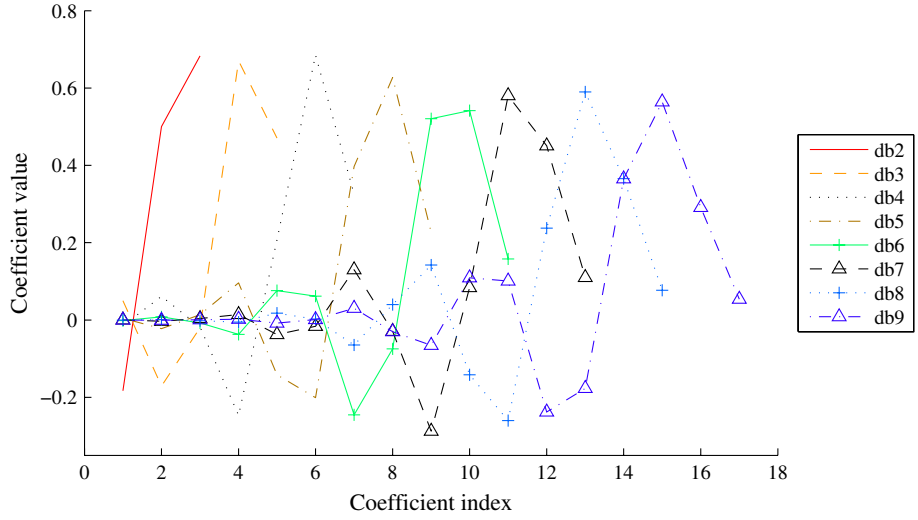

Fig. 10. Coefficients of the $\tilde{G}_0(z)$ factored polynomials for the Daubechies family.

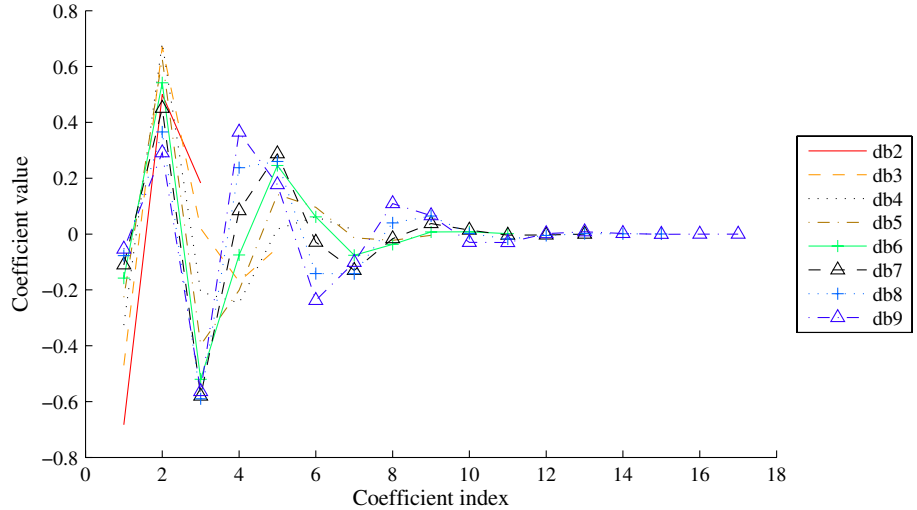

Fig. 11. Coefficients of the $\tilde{H}_0(z)$ factored polynomials for the Daubechies family.

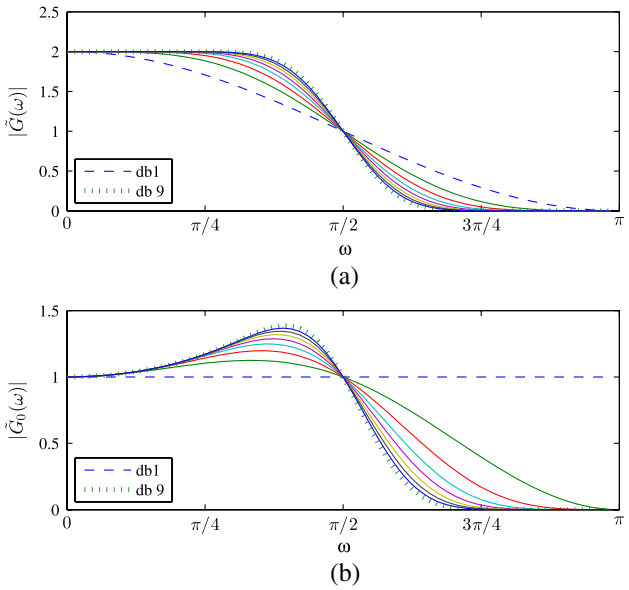

Fig. 12. (a) Digital frequency response of $\tilde{G}(z)$ for the Daubechies family. The frequency response for $\tilde{H}(z)$ would be mirrored at $\pi/2$. (b) The digital frequency response of $\tilde{G}_0(z)$ for the Daubechies family. The frequency response for $\tilde{H}_0(z)$ would be mirrored at $\pi/2$. The filtering improvement can be readily seen.

implementation of treating the data as periodic. The filter coefficients are not symmetric about their midpoint. The filters $\tilde{G}_0(z)$, $\tilde{H}_0(z)$, $G_0(z)$, and $H_0(z)$ are always shorter in length by 1.

These factored polynomials of the wavelet factoring offer the same characteristics as the other approaches, while also fitting into the wavelet technique. Longer polynomials can smooth the noise, but the choice of filter length should be

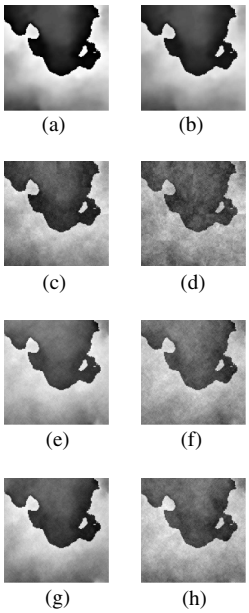

Fig. 13. (a) Original 128×128 wavefront; the remaining images are all reconstructed with (b) the Haar wavelet (the result is the same as it would be for [20]), (c) the 10 dB SNR Haar wavelet, (d) the 3 dB SNR Haar wavelet, (e) the 10 dB SNR with the Daubechies 3 wavelet, (f) the 10 dB SNR with the Daubechies 3 wavelet, (g) the 10 dB SNR with the Daubechies 9 wavelet, and (h) the 3 dB SNR with the Daubechies 9 wavelet.

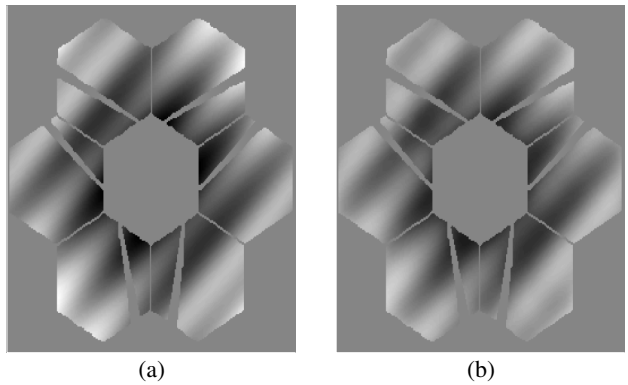

Fig. 14. (a) Original 256×256 wavefront with a telescope mask applied and (b) the reconstructed wavefront using the Daubechies 3 wavelet.

considered against the dimension length of the data. Having a large filter length but using smaller-sized data does not yield better results.

The frequency response for the Daubechies family is shown in Fig. 12, which is also called a Max-flat filter. By increasing the filter length, the rejection band performance is improved. The noise has an impact on each of the four channels (LL, LH, HL, and HH). This improved noise rejection implies that the noise will be diminished on a subset of the channels. When we also consider Shannon entropy, it is more important to have less noise on the LL channel, since it contains more information about the nature of the wavefront.

As AO systems increase in size, and therefore also the density of actuators and sensors, the larger filters are more robust than the Haar wavelet and are an appropriate choice. For example, in Fig. 13, we show the results of several reconstructions using the Daubechies family wavelets with 10 and 3 dB signal-to-noise ratios (SNRs).

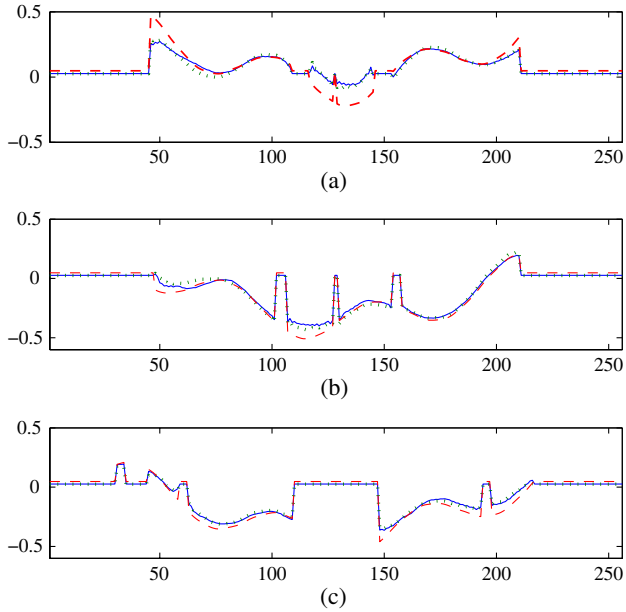

Fig. 15. Rows (a) 220, (b) 177, and (c) 90 from Fig. 14 are shown. In each plot, the dashed curve shows the original wavefront, compared against the reconstructed wavefront shown by the solid curve for Daubechies 3 and by the dotted curve for Daubechies 9.

Using only the Haar wavelet, the resulting reconstruction contains a 2×2 checkerboard pattern. The pattern is also apparent at a larger resolution in Figs. 13(c) and 13(d). With the longer wavelet lengths, we are able to have a smoothing effect on the result, as shown in Figs. 13(e)–13(h). Hampton *et al.* perform smoothing using an iterative Poisson solver in [22], which relies on having a previously reconstructed wavefront as an estimate and gradient data that are independent from the estimate. In our work, we are able to provide the smoothing effect from longer filter lengths, which can be seen in comparing Figs. 13(e)–13(g) or 13(f)–13(h).

D. Telescope Apertures with Obscurations

In the previous section, we provided example results using a square aperture. We now consider a realistic segmented mirror telescope scenario where there is an outer edge that is nonsquare and central obscuration by a secondary mirror and its support structure. We simulated this by generating data on a square aperture and then using zero value entries outside of the telescope aperture mask.

In Fig. 14, the algorithm is applied to simulated data for a notional segmented telescope system. We do not use any boundary correction or modification of the measured wavefront data, and the result is still successful in reconstructing the wavefront. In Fig. 15, we plot the 256 pixels across a row for the original wavefront in comparison with two reconstructions using the Daubechies 3 and Daubechies 9 wavelets. The reconstruction has errors near the boundary edges. Since the Daubechies 3 wavelet is shorter in filter length, it is able to converge to the actual wavefront values closer to the edge than the Daubechies 9. The Daubechies 9 wavelet also has more smoothing than the Daubechies 3 due to increased filter length, and its result has less error in reconstruction when far enough from the edges that they have no influence.

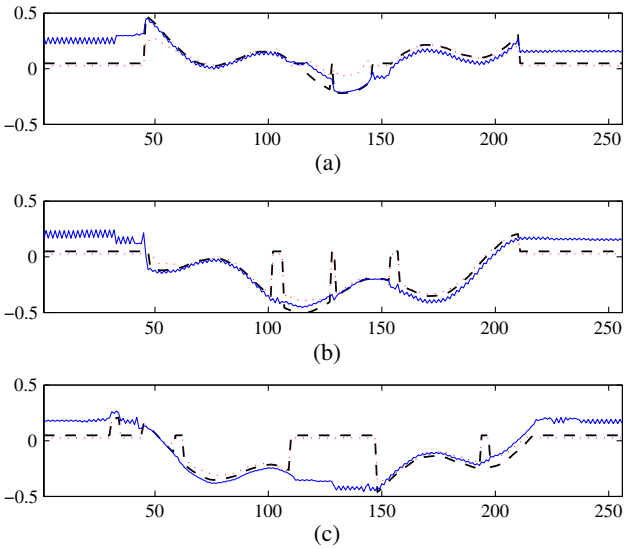

Fig. 16. (a)–(c) Three rows from Fig. 14 are shown after applying the boundary correction. In each plot, the dashed curve shows the original wavefront, compared against the reconstructed wavefront shown by the dotted curve for Daubechies 3 and by the solid curve for Daubechies 3 that has the boundary correction applied. The comparison of these results with Fig. 15 shows improvement in the result inside the aperture boundary.

Section 4 derived an additional correction that can be applied for errors due to the boundary. In Fig. 16, the corrected reconstructed wavefront can be compared to the original wavefront and the wavefront reconstructed with the algorithm of Section 3 only. The improved performance near the boundary edge is apparent. In addition, the correction also estimates the wavefront hidden underneath the structural support of the secondary mirror.

6. CONCLUSION

This paper provides a new derivation of wavelet phase reconstruction that uses the wavelet families with the orthogonal property. These families include the Haar, Daubechies, and biorthogonal wavelets. Filters with a longer region of support are able to smooth out measurement noise. The use of operator notation simplifies the written expressions of the channel definitions. The ability of a reconstruction algorithm to be computationally efficient as the density of actuators or sensors increases is important for future AO systems.

APPENDIX A: FURTHER DETAILS

1. High-Order Wavelet Simplification Proof

This proof shows how the results of Eq. (9) are determined. We start with the definition

$$g(-z^N) \triangleq \frac{1 - z^{-N}}{\sqrt{2}} \tag{A1}$$

and the definition of the geometric series

$$\sum_{\ell=0}^{N-1} z^{-\ell} \triangleq \frac{1 - z^{-N}}{1 - z^{-1}}. \tag{A2}$$

We immediately observe that Eqs. (A1) and (A2) can be combined:

$$g(-z^N) = \frac{1 - z^{-N}}{\sqrt{2}} = \frac{\left(\sum_{\ell=0}^{N-1} z^{-\ell}\right)(1 - z^{-1})}{\sqrt{2}} = \left(\sum_{\ell=0}^{N-1} z^{-\ell}\right) g(-z). \tag{A3}$$

We have now shown the first result. The second result takes some manipulation similar to the concept of polyphase decomposition, where we split the sequence up into an even and an odd component. We proceed from the result of Eq. (A3) in

$$\begin{aligned}\left(\sum_{\ell=0}^{N-1} z^{-\ell}\right) g(-z) &= \left(\sum_{\ell=0}^{\frac{N}{2}-1} z^{-2\ell} + z^{-2\ell-1}\right) g(-z) \\ &= \left((1 + z^{-1}) \sum_{\ell=0}^{\frac{N}{2}-1} z^{-2\ell}\right) g(-z) \\ &= \left(\sum_{\ell=0}^{\frac{N}{2}-1} z^{-2\ell}\right) \sqrt{2} g(z) g(-z).\end{aligned} \tag{A4}$$

The first simplification is the realization that the sum of the two sequences can be factored to $1 + z^{-1}$. The final factoring

swaps with the Haar scaling function and needs a $\sqrt{2}$ to cancel the denominator.

2. Iteration for Level k

After the second iteration, there are two unknown quantities $\phi^2_{LL/L}$ and $\phi^2_{LL/H}$. We now seek to generalize the formulas for each level $k \geq 2$. Until the final iteration, there will still be two unknown quantities. We first write out the formulas:

$$\begin{aligned}
\phi^k_{LH/L} &= (D_2D_1\tilde{H}(z_2)\tilde{G}(z_1))(D_2D_1\tilde{G}(z_2)\tilde{G}(z_1))^{k-2} \\
&\quad \ldots(D_2D_1\tilde{G}(z_2)\tilde{G}(z_1))\Phi, \\
\phi^k_{HL/L} &= (D_2D_1\tilde{G}(z_2)\tilde{H}(z_1))(D_2D_1\tilde{G}(z_2)\tilde{G}(z_1))^{k-2} \\
&\quad \ldots(D_2D_1\tilde{G}(z_2)\tilde{G}(z_1))\Phi, \\
\phi^k_{HH/L} &= (D_2D_1\tilde{H}(z_2)\tilde{H}(z_1))(D_2D_1\tilde{G}(z_2)\tilde{G}(z_1))^{k-2} \\
&\quad \ldots(D_2D_1\tilde{G}(z_2)\tilde{G}(z_1))\Phi. \qquad \text{(A5)}
\end{aligned}$$

The intent of the exponential notation is that the operations inside occur $k-2$ times. We choose to express these equations as three groups, since the left group will be used to modify the right group. Again we will factor $\tilde{H}(z)$ on the left side, then move $g(-z)$ to the right. As it swaps position with the downsampling operators, the noble identities will apply, resulting in $g(-z^{2^{k-1}})$. Then the high-order filter will be simplified to a delayed summation of the first-order filter. The relationship to the slope measurements can then be made. The end result for the LL data is

$$\begin{aligned}
\phi^k_{LH/L} &= (D_2D_1\tilde{H}_0(z_2)\tilde{G}(z_1))(D_2D_1\tilde{G}(z_2)\tilde{G}(z_1))^{k-2} \\
&\quad \ldots(D_2D_1\tilde{G}(z_2)\tilde{G}_0(z_1))\left(\left(\sum_{\ell=0}^{2^{k-1}-1} z_2^{-\ell}\right)X_F\right), \\
\phi^k_{HL/L} &= (D_2D_1\tilde{G}(z_2)\tilde{H}_0(z_1))(D_2D_1\tilde{G}(z_2)\tilde{G}(z_1))^{k-2} \\
&\quad \ldots(D_2D_1\tilde{G}_0(z_2)\tilde{G}(z_1))\left(\left(\sum_{\ell=0}^{2^{k-1}-1} z_1^{-\ell}\right)Y_F\right), \qquad \text{(A6)}
\end{aligned}$$

with a combination summation for the HH/L channel:

$$\begin{aligned}
\phi^k_{HH/L} &= \frac{1}{2}(D_2D_1\tilde{H}_0(z_2)\tilde{H}(z_1))(D_2D_1\tilde{G}(z_2)\tilde{G}(z_1))^{k-2} \\
&\quad \ldots(D_2D_1\tilde{G}(z_2)\tilde{G}_0(z_1))\left(\left(\sum_{\ell=0}^{2^{k-1}-1} z_2^{-\ell}\right)X_F\right) \\
&\quad + \frac{1}{2}(D_2D_1\tilde{H}(z_2)\tilde{H}_0(z_1))(D_2D_1\tilde{G}(z_2)\tilde{G}(z_1))^{k-2} \\
&\quad \ldots(D_2D_1\tilde{G}_0(z_2)\tilde{G}(z_1))\left(\left(\sum_{\ell=0}^{2^{k-1}-1} z_1^{-\ell}\right)Y_F\right). \qquad \text{(A7)}
\end{aligned}$$

The HH data is again developed through the same manner and results in definitions with some slight differences:

$$\begin{aligned}
\phi^k_{LH/H} &= (D_2D_1\tilde{H}_0(z_2)\tilde{G}(z_1))(D_2D_1\tilde{G}(z_2)\tilde{G}(z_1))^{k-2} \\
&\quad \ldots(D_2D_1\tilde{H}(z_2)\tilde{H}_0(z_1)) \\
&\quad \ldots\left(\left(\sum_{\ell=0}^{2^{k-2}-1} z_2^{-2\ell}\right)\sqrt{2}g(-z_2)Y_F\right), \\
\phi^k_{HL/H} &= (D_2D_1\tilde{G}(z_2)\tilde{H}_0(z_1))(D_2D_1\tilde{G}(z_2)\tilde{G}(z_1))^{k-2} \\
&\quad \ldots(D_2D_1\tilde{H}_0(z_2)\tilde{H}(z_1)) \\
&\quad \ldots\left(\left(\sum_{\ell=0}^{2^{k-2}-1} z_1^{-2\ell}\right)\sqrt{2}g(-z_1)X_F\right), \qquad \text{(A8)}
\end{aligned}$$

and the final channel, HH/H, is again defined as a combination:

$$\begin{aligned}
\phi^k_{HH/H} &= \frac{1}{2}(D_2D_1\tilde{H}_0(z_2)\tilde{H}(z_1))(D_2D_1\tilde{G}(z_2)\tilde{G}(z_1))^{k-2} \\
&\quad \ldots(D_2D_1\tilde{H}(z_2)\tilde{H}_0(z_1)) \\
&\quad \ldots\left(\left(\sum_{\ell=0}^{2^{k-2}-1} z_2^{-2\ell}\right)\sqrt{2}g(-z_2)Y_F\right) \\
&\quad + \frac{1}{2}(D_2D_1\tilde{H}(z_2)\tilde{H}_0(z_1))(D_2D_1\tilde{G}(z_2)\tilde{G}(z_1))^{k-2} \\
&\quad \ldots(D_2D_1\tilde{H}_0(z_2)\tilde{H}(z_1)) \\
&\quad \ldots\left(\left(\sum_{\ell=0}^{2^{k-2}-1} z_1^{-2\ell}\right)\sqrt{2}g(-z_1)X_F\right). \qquad \text{(A9)}
\end{aligned}$$

The summations represent either a zero-padded shift or a circular shift of the data, and it should match the preferred implementation of how the sequences are treated for boundary conditions.

ACKNOWLEDGMENTS

The authors acknowledge email communication with P. Hampton. This research was performed with the Adaptive Optics Center of Excellence in National Security, located at the Naval Postgraduate School. T. W. Axtell was funded by the Department of Defense SMART Scholarship and Space and Naval Warfare Command. Gratitude is also expressed to the anonymous reviewers for their comments, which were crucial for improving the quality of the paper.

REFERENCES

1. F. Roddier, *Adaptive Optics in Astronomy* (Cambridge University, 1999).
2. P. Y. Bely, ed., *The Design and Construction of Large Optical Telescopes* (Springer, 2003).
3. W. H. Southwell, "Wave-front estimation from wave-front slope measurements," J. Opt. Soc. Am. **70**, 998–1006 (1980).
4. L. A. Poyneer, D. T. Gavel, and J. M. Brase, "Fast wave-front reconstruction in large adaptive optics systems with use of the Fourier transform," J. Opt. Soc. Am. A **19**, 2100–2111 (2002).
5. D. L. Fried, "Least-square fitting a wave-front distortion estimate to an array of phase-difference measurements," J. Opt. Soc. Am. **67**, 370–375 (1977).
6. R. H. Hudgin, "Wave-front reconstruction for compensated imaging," J. Opt. Soc. Am. **67**, 375–378 (1977).
7. J. Herrmann, "Least-squares wave front errors of minimum norm," J. Opt. Soc. Am. **70**, 28–35 (1980).

8. K. Freischlad, "Wavefront reconstruction from noisy slope or difference data using the discrete Fourier transform," Proc. SPIE **551**, 74–80 (1985).
9. L. Gilles, C. R. Vogel, and B. L. Ellerbroek, "Multigrid preconditioned conjugate-gradient method for large-scale wave-front reconstruction," J. Opt. Soc. Am. A **19**, 1817–1822 (2002).
10. D. G. MacMartin, "Local, hierarchic, and iterative reconstructors for adaptive optics," J. Opt. Soc. Am. A **20**, 1084–1093 (2003).
11. L. Gilles, "Sparse minimum-variance open-loop reconstructors for extreme adaptive optics: order N multigrid versus preordered Cholesky factorization," Proc. SPIE **5169**, 201–205 (2003).
12. C. R. Vogel, "Sparse matrix methods for wavefront reconstruction, revisited," Proc. SPIE **5490**, 1327–1335 (2004).
13. C. R. Vogel and Q. Yang, "Multigrid algorithm for least-squares wavefront reconstruction," Appl. Opt. **45**, 705–715 (2006).
14. C. Béchet, M. Tallon, and E. Thiébaut, "FRIM: minimum-variance reconstructor with a fractal iterative method," Proc. SPIE **6272**, 62722U (2006).
15. E. Thiébaut and M. Tallon, "Fast minimum variance wavefront reconstruction for extremely large telescopes," J. Opt. Soc. Am. A **27**, 1046–1059 (2010).
16. J. Herrmann, "Phase variance and Strehl ratio in adaptive optics," J. Opt. Soc. Am. A **9**, 2257–2258 (1992).
17. M. Rosensteiner, "Cumulative reconstructor: fast wavefront reconstruction algorithm for extremely large telescopes," J. Opt. Soc. Am. A **28**, 2132–2138 (2011).
18. C. C. de Visser and M. Verhaegen, "Wavefront reconstruction in adaptive optics systems using nonlinear multivariate splines," J. Opt. Soc. Am. A **30**, 82–95 (2013).
19. F. U. Dowla, "Fast Fourier and wavelet transforms for wavefront reconstruction in adaptive optics," Proc. SPIE **4124**, 118–127 (2000).
20. P. J. Hampton, P. Agathoklis, and C. Bradley, "A new wave-front reconstruction method for adaptive optics systems using wavelets," IEEE J. Sel. Top. Signal Process. **2**, 781–792 (2008).
21. P. J. Hampton, "Robust order N wavelet filterbanks to perform 2-D numerical integration directly from partial difference or gradient measurements," Ph.D. thesis (University of Victoria, 2009).
22. P. J. Hampton, P. Agathoklis, R. Conan, and C. Bradley, "Closed-loop control of a woofer-tweeter adaptive optics system using wavelet-based phase reconstruction," J. Opt. Soc. Am. A **27**, A145–A156 (2010).
23. D. E. Dudgeon and R. M. Mersereau, *Multidimensional Digital Signal Processing* (Prentice-Hall, 1984).
24. W. L. Briggs, V. E. Henson, and S. F. McCormick, *A Multigrid Tutorial* (SIAM, 2000).
25. P. P. Vaidyanathan, *Multirate Systems and Filter Banks* (Prentice-Hall, 1993).
26. C. Shannon, "The mathematical theory of communication," Bell Syst. Tech. J. **27**, 379–423, 623–656 (1948).
27. A. Haar, "Zur Theorie der orthogonalen Funktionensysteme," Ph.D. thesis (University of Göttingen, 1909).